nature communications

Article

https://doi.org/10.1038/s41467-025-58590-z

Nickel Ion Induced Multistage Assembly of Th_{13} Cluster

Received: 6 August 2024

Accepted: 25 March 2025

Published online: 29 April 2025

Check for updates

Kong-Qiu Hu[1,5] ✉, Jun-Xi Wang[1,2,5], Qun-Yan Wu[1,5], Zhi-Wei Huang[1], Zhi-Heng Zhou[1,2], Jin-Dong Wang[1], Xiao-Bo Li[1], Ji-Pan Yu[1], Zhi-Hui Zhang[3], Lei Mei[1], Yong-De Yan[2] & Wei-Qun Shi[1,4] ✉

Clusters have proven useful models to elucidate the correlation between macroscopic properties and microstructures. However, the actinide clusters still remain much less developed compared to the splendid and systematic works of other members of this family. Here we show the synthesis of a tetra-shell mixed-metal cluster $[ThO_8@Th_{12}(OH)_{24}@Ni_6(H_2O)_{18}@(sba)_{12}]$ (IHEP-25, H_2sba: 2-sulfobenzoic acid) with the strategic introduction of competitive Ni^{2+} ions. A cluster-based framework (IHEP-28), featuring a 2D honeycomb network and demonstrating excellent stability, has been constructed through the multistage assembly of IHEP-25, facilitated by the introduction of cationic cluster $[Na_4(OH)_3(H_2O)_3]^+$. IHEP-28 acts as a highly effective visible light-driven photocatalyst for CO_2 reduction. This study demonstrates that the incorporation of heterometal ions not only alters the hydrolysis patterns of actinide metal ions, resulting in the formation of new actinide clusters, but also broadens their potential applications.

Clusters, serving as intermediaries between discrete metal ions and bulk materials, present perfect models to elucidate the correlation between macroscopic properties and microstructures, leading to the synthesis and comprehensive characterization of numerous polynuclear metal clusters involving transition, main-group, and lanthanide metals[1–12]. In contrast, the exploration of actinide clusters lags behind[13]. In recent years, with the development of the nuclear industry, actinide clusters have gradually attracted attention due to their potential applications in managing nuclear waste and mitigating radioactive pollution. For instance, under neutral and alkaline conditions, the pronounced propensity of actinides, especially their hypervalent ions, for hydrolysis can lead to the genesis of soluble polynuclear species. These species are of paramount importance in understanding the environmental transport and migration of radionuclides[14–16]. The methodical investigation of actinide clusters thus offers critical insights for precisely depicting the mobility of radionuclides in environmental matrices. Against this backdrop, several notable actinide clusters have been synthesized and detailed, including U(IV)-based clusters such as $[U_{16}]$, $[U_{24}]$, $[U_{38}]$[17], an assortment of uranyl-peroxide clusters[18–25], the mixed-valent cluster $[U^V(U^{VI}O_2)_8]$[26], and transuranic clusters $[Pu_{38}]$[27,28] and $[Np_{38}]$[29], showcasing significant strides in the field.

Thorium is gaining attention as a potential new source of nuclear energy, especially with the development of Molten Salt Reactors (MSR)[30–32]. Consequently, the chemistry of thorium has become increasingly significant in recent years[33–37]. The synthesis and structural characterization of polynuclear thorium clusters, in particular, play a crucial role in enhancing our understanding of the structures and properties of thorium-based materials, including thorium colloids and thorium-based nuclear fuels. While there have been recent advances in the chemistry of uranium clusters, the study of thorium (Th) clusters remains comparatively underdeveloped[13,34–42]. Due to the acidity and high charge density, the propensity of Th^{4+} ions to undergo hydrolysis typically leads to the formation of lower-nuclearity clusters or ThO_2

[1]Laboratory of Nuclear Energy Chemistry, Institute of High Energy Physics, Chinese Academy of Sciences, Beijing, China. [2]Yantai Research Institute, Harbin Engineering University, Yantai, Shandong, China. [3]Jiangsu Key Laboratory of Advanced Catalytic Materials and Technology, Advanced Catalysis and Green Manufacturing Collaborative Innovation Center, Changzhou University, Changzhou, China. [4]School of Nuclear Science and Engineering, and Key Laboratory of Nuclear Power Systems and Equipment/Ministry of Education, Shanghai Jiao Tong University, Shanghai, China. [5]These authors contributed equally: Kong-Qiu Hu, Jun-Xi Wang, Qun-Yan Wu. ✉e-mail: hukq@ihep.ac.cn; shiwq@sjtu.edu.cn

nanoparticles[23,43–53]. A reasonable strategy for synthesizing large-nuclearity thorium clusters involves the introduction of competitive metal ions. These ions, alongside organic or inorganic ligands, can serve as terminating agents that prevent the aggregation of actinide polynuclear species into stable colloids[54,55]. By varying the types of competitive metal ions introduced, it's possible to tailor the hydrolysis and condensation behaviors of actinides, potentially leading to the formation of mixed-metal clusters with greater nuclearity and size. Furthermore, considering the complexity of natural environmental systems, understanding the formation processes and structural traits of various mixed-metal clusters can aid in predicting the occurrence, migration pathways, and concentration mechanisms of actinide elements under diverse environmental conditions[56–61]. This insight is crucial for advancing research in environmental science and geology. Meanwhile, it can expand the potential applications of actinide materials[62].

As a proof-of-concept, herein we report the synthesis and characterization of a mixed-metal cluster, $[Th_{13}Ni_6O_8(OH)_{24}(H_2O)_{18}(sba)_{12}]$ (IHEP-25, H_2sba: 2-sulfobenzoic acid). At its core, IHEP-25 features a $[Th_{13}O_8(OH)_{24}]$ structure, analogous to the classical α-Keggin type molecule. By modifying the reaction conditions, some of the surface solvent ligands can be exchanged, resulting in the formation of three additional $[Th_{13}Ni_6]$ clusters: $[Th_{13}Ni_6(O)_8(OH)_{24}(sba)_{12}(H_2O)_{12}(CH_3CN)_6]$ (IHEP-26), $[Th_{13}Ni_6(O)_8(OH)_{24}(sba)_{12}(H_2O)_{18}][Th_{13}Ni_6(O)_8(OH)_{24}(sba)_{12}(H_2O)_{12}(CH_3CN)_6]$ (IHEP-27) and $[Th_{13}Ni_6(O)_8(OH)_{24}(sba)_{12}(H_2O)_{10}(CH_3CN)_2]$ (IHEP-31). Furthermore, the stable $[Th_{13}Ni_6]$ cluster can also assemble into a 2D honeycomb net structure, IHEP-28 $\{[Th_{13}Ni_6(O)_8(OH)_{24}(sba)_{14}(H_2O)_{12}(CH_3COO)_2(CH_3CN)_2]_3[Na_4(OH)_3(H_2O)_3]_2\}_n$, induced by the cation cluster $[Na_4(OH)_3(H_2O)_3]^+$. IHEP-28 demonstrates exceptional stability in air and various solvents and serves as an effective CO_2 reduction photocatalyst in the visible light region.

Results

Structural characterization

Single-crystal X-ray diffraction reveals that IHEP-25 crystallizes in the cubic space group $Pn\bar{3}n$ (Supplementary Table S1). As shown in Fig. 1a and Supplementary Fig. S1, the asymmetric unit of IHEP-25 contains three crystallographically independent Th atoms, one Ni atom, six O^{2-}/OH^- anions, two deprotonated 2-sulfobenzoic acid anion ligands (sba^{2-}) and three coordinated H_2O. In this unit, Th3 is located at the special position of the symmetry axis with a position occupancy of 1/6, while the other two Th atoms have full occupancies 1.0. Through an axisymmetric operation the complete $[Th_{13}Ni_6(O)_8(OH)_{18}(OH)_6(sba)_{12}(H_2O)_{18}]$ cluster structure of IHEP-25 is obtained (Fig. 1b). The entire structure of IHEP-25 is organized into four concentric shells (Supplementary Fig. S2). In the innermost shell, a Th atom (Th2) resides at the center, coordinated by eight μ_4-O^{2-}, forming an approximate cube with O···O distances ranging from 2.7532 Å to 2.7908 Å (Fig. 1c, f and Supplementary Figs. S3 and S4a). The cube is enveloped by 12 Th atoms as the second shell, as shown in

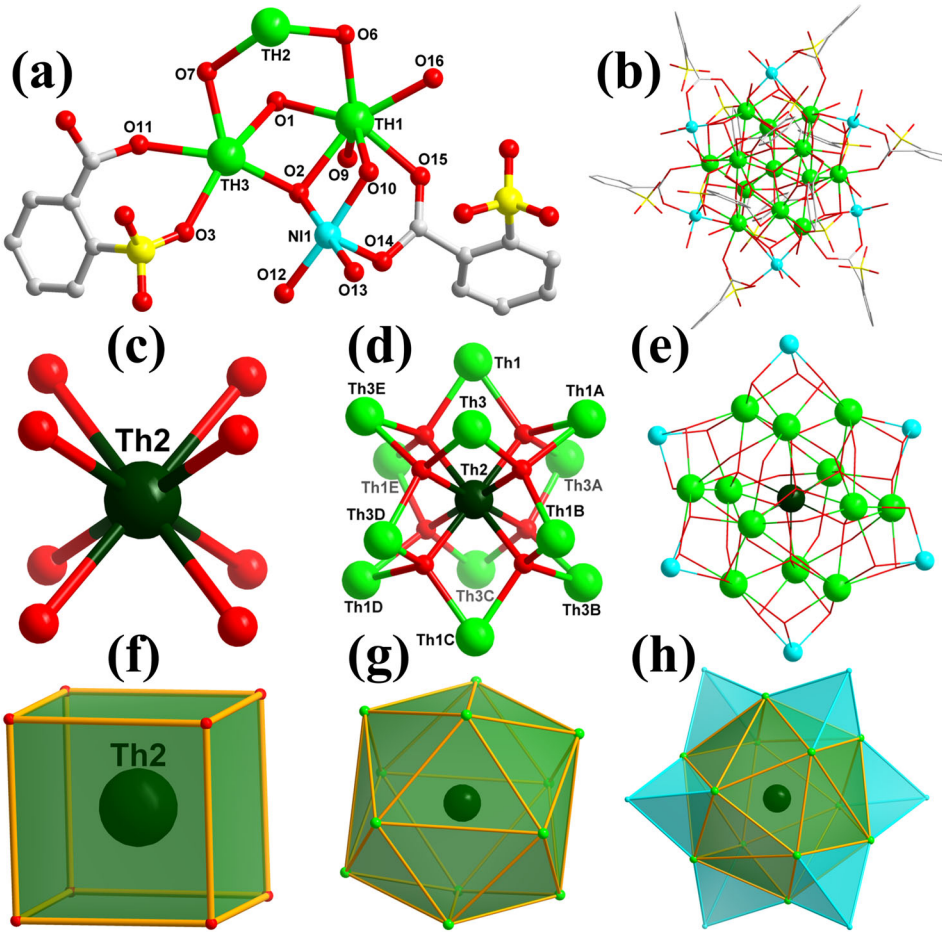

Fig. 1 | The structure of IHEP-25. a The asymmetric unit of IHEP-25. **b** The whole structure of IHEP-25. **c** Th2 atom is coordinated by eight μ_4-O^{2-} to from an approximate cube. **d** The $[Th_{13}]$ core structure of IHEP-25. **e** The $[Th_{13}Ni_6]$ core structure of IHEP-25. **f** The simplified cubic geometrical configuration of Th2. **g** Twelve Th atoms are bridged to each other by 30 oxygen atoms to form an approximate Archimedean Solid icosahedron structure. **h** Six $NiTh_3$ units interconnect through a vertex-sharing mode and integrated onto the $[Th_{13}]$ icosahedron surface via a face-sharing approach. Color scheme: Th, green and dark green; Ni, cyan; C, gray; O, red; S, yellow. H atoms are omitted for clarity.

Fig. 1d. These 12 Th atoms are interconnected by 30 oxygen atoms, stemming from 18 μ_3-OH^-, 6 μ_2-OH^- and 6 sba^{2-} ligands (Supplementary Fig. S3), constructing an approximate Archimedean Solid icosahedron structure (Fig. 1g), with Th···Th distances varying from 3.8140 Å to 4.7679 Å (Supplementary Fig. S4b). The central $[ThO_8@Th_{12}(OH)_{24}]^{12+}$ core is reminiscent of an α-Keggin type molecule. While such cores have been noted in various metal clusters[9], this report marks the first appearance of such a core structure in thorium clusters. Furthermore, six Ni atoms are uniformly distributed around the Th_{13} cluster, forming a six-membered ring with a chair conformation as the third shell, with Ni···Ni distance of 6.7329 Å (Supplementary Fig. S4c and S4d). Each Ni atom is linked to three Th atoms via three μ_3-OH^- ligands (Fig. 1e) to form a compressed tetrahedral $NiTh_3$ structure. These six $NiTh_3$ units interconnect through a vertex-sharing mode and integrated onto the $[Th_{13}]$ icosahedron surface via a face-sharing approach (Fig. 1h). The fourth shell of IHEP-25 is consisting of 12 sba^{2-} ligands, which serve to shield the heterometal clusters from further hydrolysis and prevent polymer formation, resulting in the matryoshka nanocluster $[ThO_8@Th_{12}(OH)_{24}@Ni_6(H_2O)_{18}@(sba)_{12}]$ (Fig. 1b and Supplementary Fig. S2d). Based on the differing coordination interactions between the sba^{2-} ligands and metal ions, the twelve coordinating ligands of IHEP-25 are categorized into two groups with coordination modes of μ_2-$\eta^1\eta^2\eta^1$ and μ_2-$\eta^1\eta^1$ (Supplementary Fig. S5). The coordination modes of all the ligands involved in IHEP-25 have been collected in Table 1. As shown in Supplementary Fig. S6, each $[Th_{13}Ni_6]$ cluster is connected to six adjacent equivalent clusters through hydrogen bonding (C-H···O-S, C-H···O-C, O-H···O-S), forming a 3D supramolecular structure.

Theoretical calculation of mixed-metal $[Th_{13}Ni_6]$ clusters

The structures of the inner cores $[Th_{13}(O)_8(OH)_{24}]^{12+}$ cluster and $[Th_{13}(O)_8(OH)_{24}Ni_6(sba)_{12}(H_2O)_{18}]$ molecule were explored using the scalar-relativistic density functional theory (DFT) to explore the electronic structures. The detail computational methods are provided in SI, and the optimized structures are shown in Supplementary Fig. S15. The front molecular orbitals (MOs) and the corresponding energy levels of $[Th_{13}(O)_8(OH)_{24}]^{12+}$ are provided in Fig. 2. The energy gap between the highest occupied MO (HOMO) and the lowest unoccupied MO (LUMO) of $[Th_{13}(O)_8(OH)_{24}]^{12+}$ is 4.03 eV, which is significant larger than that of Au_{20} (1.82 eV)[63] and C_{60} (1.57 eV)[64] clusters, which reflects that the $[Th_{13}(O)_8(OH)_{24}]^{12+}$ cluster is highly stability. The energy level of MOs obviously shows three parts in Fig. 2, the lowest band is Th 6 d and O 2p orbitals, the middle band is mainly O 2p orbitals, while for the highest band is dominated by Th 6 d orbitals. Moreover, the six lower HOMOs (HOMO-66 - HOMO-71) appear obvious interactions between Th and O atoms. The analysis of the electron localization function (ELF) of the $[Th_{13}(O)_8(OH)_{24}]^{12+}$ cluster with three planes, including different Th-O bonds, is displayed in Supplementary Fig. S16. There is clear interaction between the Th and O atom with more electron density, which also implies the stable electronic structure. In addition, the electronic structure of $[Th_{13}(O)_8(OH)_{24}Ni_6(H_2O)_{18}(sba)_{12}]$ is also explored at the same level of theory, and the front MOs are showed in Supplementary Fig. S17. The HOMO-LUMO gap (2.61 eV) of $[Th_{13}(O)_8(OH)_{24}Ni_6(H_2O)_{18}(sba)_{12}]$ is smaller than that of $[Th_{13}(O)_8(OH)_{24}]^{12+}$ core because the HOMOs of former are contributed by the Ni 3 d orbitals, which suggests that Ni^{2+} has the potential to serve as the catalytic active center of $[Th_{13}(O)_8(OH)_{24}Ni_6(H_2O)_{18}(sba)_{12}]$ cluster.

Controlling the Secondary Assembly of $[Th_{13}Ni_6]$ Cluster

Similar to other stable clusters, the surface ligands of the $[Th_{13}Ni_6]$ cluster are exchangeable[65]. By modifying the reaction conditions, three additional $[Th_{13}Ni_6]$ clusters, IHEP-26, IHEP-27, and IHEP-31, have been synthesized. As shown in Supplementary Figs. S7 and S32, the asymmetric unit of IHEP-26 constitutes half of a $[Th_{13}Ni_6]$ cluster, presenting three types of Ni^{2+} cations characterized by various coordination modes. Ni1 is bonded to three OH^-, two sba^{2-} ligands, and one H_2O molecule. Ni2 is coordinated by three OH^-, two H_2O, and one CH_3CN molecule. The coordination sphere of Ni3 is occupied by three OH^-, two CH_3CN molecules, and one sba^{2-} ligand. Consequently, the six coordinated H_2O molecules in IHEP-25 are substituted by six CH_3CN molecules, resulting in the comprehensive $[Th_{13}Ni_6(O)_8(OH)_{24}(sba)_{12}(H_2O)_{12}(CH_3CN)_6]$ cluster structure of IHEP-26 (Fig. 3a). As shown in Fig. 3b, the entire structure of IHEP-27 contains two independent $Th_{13}Ni_6$ clusters with molecule formula of $[Th_{13}Ni_6(O)_8(OH)_{24}(sba)_{12}(H_2O)_{18}][Th_{13}Ni_6(O)_8(OH)_{24}(sba)_{12}(H_2O)_{12}(CH_3CN)_6]$. One of the $Th_{13}Ni_6$ clusters matches that of IHEP-25. The other, while akin to the IHEP-25' cluster, features one of the Ni^{2+} cation coordinating H_2O molecules replaced by CH_3CN (Supplementary Fig. S8). As shown in Supplementary Fig. S9a, the asymmetric unit of IHEP-31 constitutes half of a $[Th_{13}Ni_6]$ cluster, presenting two types of Ni^{2+} cations characterized by various coordination modes. The coordination modes of Ni1 and Ni2 are similar, both are bonded to three OH^-, one sba^{2-} ligand and one H_2O molecule. Ni3 is coordinated by three OH^-, one sba^{2-} ligand, one H_2O, and one CH_3CN molecule (Supplementary Fig. S9c). The comprehensive $[Th_{13}Ni_6(O)_8(OH)_{24}(sba)_{12}(H_2O)_{10}(CH_3CN)_2]$ cluster structure of IHEP-31 is shown in Supplementary Fig. S9b.

The adaptability of the surface ligands enables the $Th_{13}Ni_6$ cluster to function as a versatile node for constructing cluster-based materials, akin to other stable clusters such as $[Fe_3]$, $[Th_6]$, $[Ag_{13}]$, and others. Illustrating its potential, the $[Th_{13}Ni_6]$ cluster can be interlinked with the $[Na_4(OH)_3(H_2O)_3]^+$ cationic cluster to forge a 2D honeycomb network, forming the foundational structure of IHEP-28 (Fig. 3c). The asymmetric unit of IHEP-28 comprises half a $[Th_{13}Ni_6]$ cluster core and a third of a $[Na_4]$ cluster core, as depicted in Supplementary Fig. S10a and S10b. The coordination environments of the metal ions and the coordination patterns of sba^{2-} ligands are detailed in Supplementary Figs. S11 and S12, respectively. While the $[Th_{13}Ni_6]$ cluster core of IHEP-28 remains consistent with those in IHEP-25, 26, 27, and 31, its surface ligands exhibit significant differences. Some of the coordinated H_2O molecules are substituted with CH_3CN molecules, CH_3COO^- ligands, and sba^{2-} ligands, culminating in the comprehensive $[Th_{13}Ni_6(O)_8(OH)_{24}(sba)_{14}(H_2O)_{12}(CH_3COO)_2(CH_3CN)_2]$ cluster structure (Supplementary Fig. S10c and S10d). Each $[Th_{13}Ni_6]$ cluster is tethered to four adjacent units via two $[Na_4]$ clusters, creating an extensive heterotrimetal honeycomb (6, 3) network (Fig. 3c and Supplementary Fig. S13) with a $[Th_{13}Ni_6]$ cluster separation of 19.1534(3) Å. The honeycomb network's minimal structural unit is composed of six $[Th_{13}Ni_6]$ clusters and six $[Na_4]$ clusters, boasting a diameter of 24.0932(4) Å (Supplementary Fig. S13b). Moreover, the adjacent 2D networks exhibit an ABCABC stacking pattern (Supplementary Fig. S13d), evolving into a 3D porous framework (Supplementary Fig. S14).

Synthetic comments

In solvothermal reactions, some organic functional groups may undergo in situ reactions due to high temperature and pressure conditions. Typical examples of such reactions include the hydrolysis of cyano and ester groups[66], as well as the oxidation of halogen groups[67]. Notably, during the synthesis of coordination polymers, it is quite common for cyano groups to hydrolyze and then coordinate with metal ions, a phenomenon that also accounts for the source of acetate ligands in IHEP-28. In addition to the aforementioned reactions, all the compounds reported in this work involve the in situ oxidation of thiol groups to sulfonate groups, a process that has been documented in several literatures[68]. In our study, we conducted a solvothermal reaction by dissolving nickel nitrate, thiosalicylic acid, and sodium hydroxide in a mixed solution of water and acetonitrile, obtaining a thiol-coupled product, 2, 2'-dithiosalicylic acid. However, when thorium nitrate was added to the reaction system, thiosalicylic acid was oxidized to 2-sulfobenzoic acid. This oxidation phenomenon may stem

https://doi.org/10.1038/s41467-025-58590-z

Table 1 | Coordination modes of all the ligands involved in IHEP-25 -IHEP-31

Ligands	Coordination modes	Compounds	Ligands	Coordination modes	Compounds
sba^{2-} (μ_2-$\eta^1\eta^2\eta^1$)	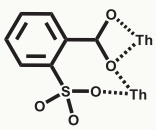	IHEP-25, IHEP-26, IHEP-27, IHEP-28, IHEP-31	O^{2-} (μ_3-O)	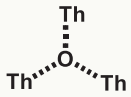	IHEP-29
sba^{2-} (μ_2-$\eta^1\eta^1$)	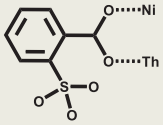	IHEP-25, IHEP-26, IHEP-27, IHEP-28	OH^- (μ_3-OH_{ThThNi})	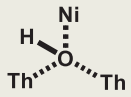	IHEP-25, IHEP-26, IHEP-27, IHEP-28, IHEP-31
sba^{2-} (μ_2-$\eta^1\eta^1\eta^1$)	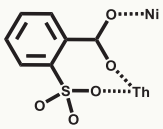	IHEP-31	OH^- (μ_2-OH_{ThTh})	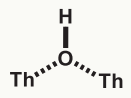	IHEP-25, IHEP-26, IHEP-27, IHEP-28, IHEP-31
sba^{2-} (μ_2-$\eta^1\eta^1$)	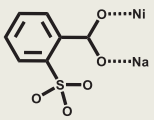	IHEP-28	OH^- (μ_2-OH_{NaNa})	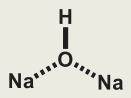	IHEP-28
sba^{2-} (μ_4-$\eta^1\eta^1\eta^1\eta^1$)	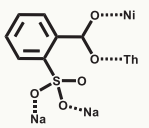	IHEP-28	OH^- (μ_3-OH_{ThThTh})	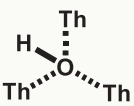	IHEP-29
sba^{2-}(μ_3-$\eta^1\eta^2\eta^1\eta^1$)	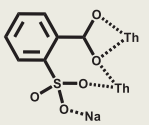	IHEP-28	H_2O	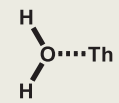	IHEP-25, IHEP-26, IHEP-27, IHEP-28
sba^{2-} (μ_3-$\eta^1\eta^1\eta^1\eta^1$)	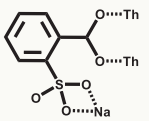	IHEP-29	H_2O	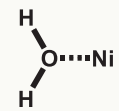	IHEP-25, IHEP-26, IHEP-27, IHEP-28, IHEP-31
sba^{2-}(μ_3-$\eta^1\eta^2\eta^1$)	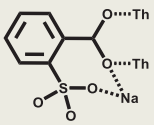	IHEP-29	H_2O	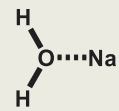	IHEP-28, IHEP-29
sba^{2-} (μ_4-$\eta^1\eta^1\eta^1\eta^1$)	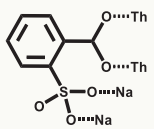	IHEP-29	CH_3CN		IHEP-26, IHEP-27, IHEP-28, IHEP-31
sba^{2-} (μ_2-$\eta^1\eta^1\eta^1$)	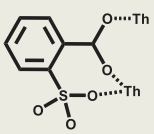	IHEP-30	CH_3COO^-	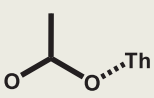	IHEP-28
O^{2-} (μ_4-O)	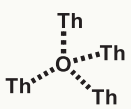	IHEP-25, IHEP-26, IHEP-27, IHEP-28, IHEP-31			

from the strong hydrolysis of Th^{4+} under high-temperature and high-pressure conditions, leading to the generation of hydrogen ions from water decomposition. This process significantly enhances the oxidizing ability of nitrate anions, thereby facilitating the oxidation of thiosalicylic acid to generate 2-sulfobenzoic acid[69].

To explore the potential formation mechanism of $[Th_{13}Ni_6]$ clusters, a series of comparative experiments were conducted. Based on the results of these experiments and the structural comparison of thorium complexes reported in this work, a possible formation mechanism for $[Th_{13}Ni_6]$ clusters was proposed (Supplementary Fig. S18). Reported thorium monomers include $Th(OH)_3^+$ and $Th(OH)_2^{2+}$, as well as dimers e.g., $Th_2(OH)_2^{6+}$, tetramers e.g., $Th_4(OH)_{12}^{4+}$, and hexamers e.g., $Th_6(\mu_3\text{-}O)_4(\mu_3\text{-}OH)_4^{12+}$, all of which are important species of thorium ions in solution[23]. In addition, the

https://doi.org/10.1038/s41467-025-58590-z

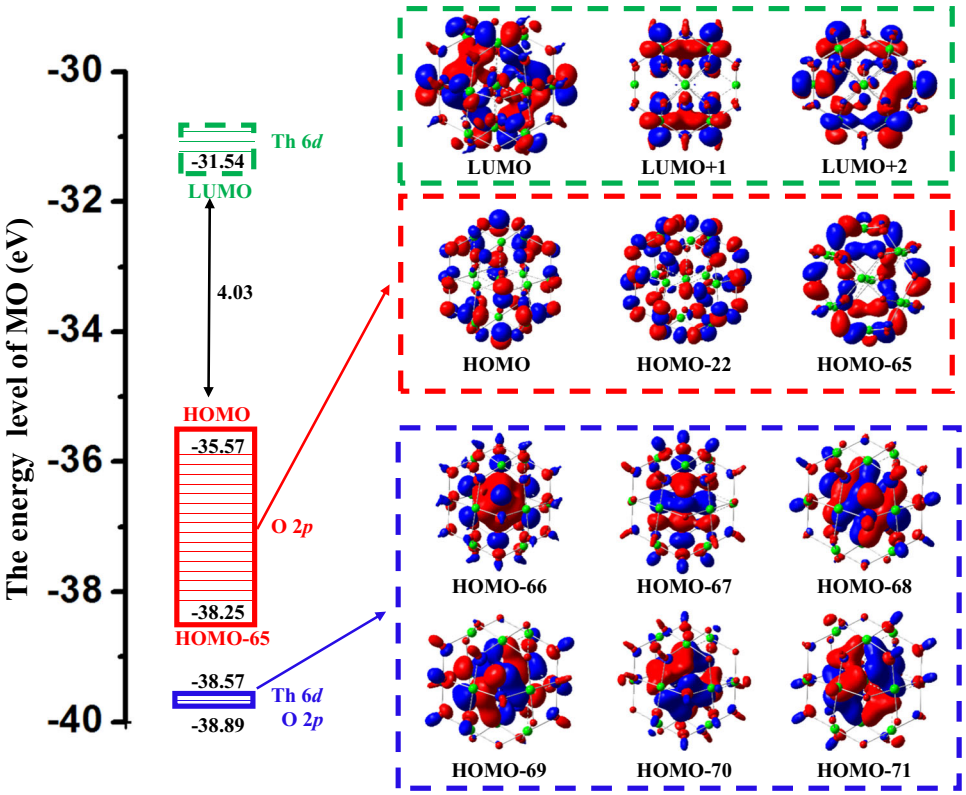

Fig. 2 | The energy gap between HOMO and LUMO of $[Th_{13}(O)_8(OH)_{24}]^{12+}$. The energy level (eV) of MOs for the inner core $[Th_{13}(O)_8(OH)_{24}]^{12+}$ cluster and the representative MOs for each energy level band at the bp86/ECP78MWB/6-31 G(d) level of theory.

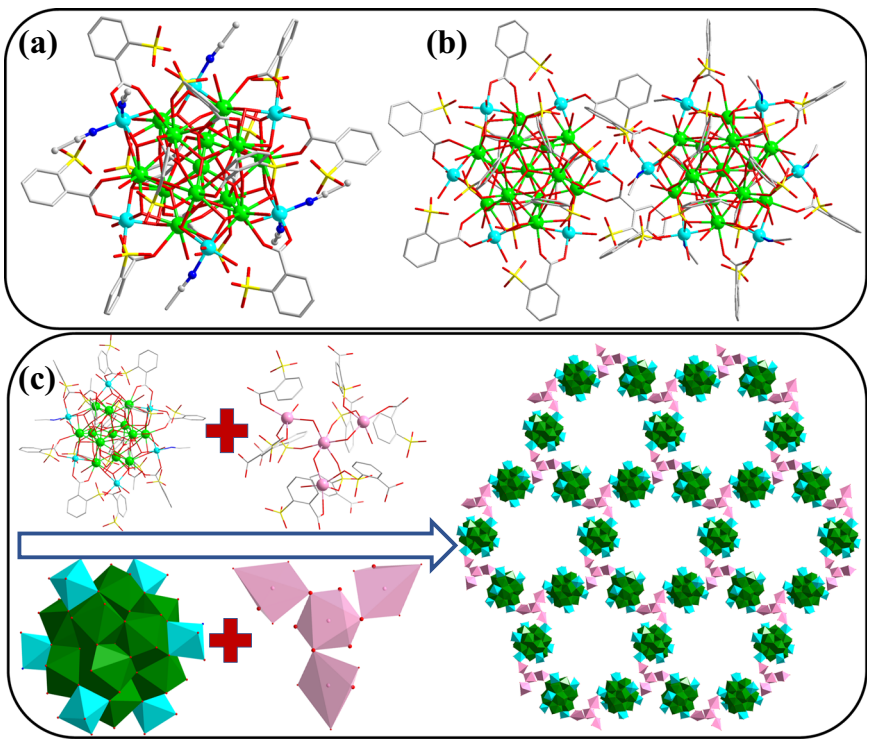

Fig. 3 | The structures of IHEP-26, IHEP-27, and IHEP-28. a The whole structure of IHEP-26. **b** The whole structure of IHEP-27. **c** The $Th_{13}Ni_6$ cation cluster can be bridged by the cationic cluster $[Na_4(OH)_3(H_2O)_3]^+$ to form the 2D honeycomb network of IHEP-28. Color scheme: Th, green; Ni, cyan; Na, pink; C, gray; O, red; N, blue; S, yellow. H atoms are omitted for clarity.

presence of carboxylate anion ligands can promote the formation of hexamer [Th_6] clusters[70–72], which is consistent with our experimental observations: in the absence of Ni^{2+} ions, Th^{4+} ions preferentially assemble with the sba^{2-} ligand to form $[Th_6(O)_4(OH)_4(sba)_{12}(H_2O)_6]$ cluster (IHEP-29, Supplementary Fig. S19). As the concentration of NaOH increases, the morphology of the [Th_6] cluster changes, accompanied by the generation of amorphous thorium hydroxide, which eventually becomes the main product. After the introduction of Ni^{2+} ions, [Th_6] clusters were no longer observed in the reaction products; instead, [$Th_{13}Ni_6$] clusters and 1D chain structure (IHEP-30) with mononuclear Th^{4+} as nodes formed. This is due to the competition between nickel ions and the [$Th_6(sba)_{12}$] cluster for the sba^{2-} ligands, leading to its dissociation into units such as [Th_5], [Th_4], and mononuclear [Th]. In a low-alkalinity environment, the dissociation products are primarily mononuclear [Th], which further form a 1D chain structure IHEP-30, $\{Th(sba)_2(H_2O)_3\}_n{\cdot}2nH_2O$ (Supplementary Fig. S20). As the alkalinity of the reaction system increases, the stability of the lacuna oligomers [Th_5] and [Th_4] is enhanced. This enhancement facilitates their secondary assembly in a co-vertex manner, resulting in the formation of an intermediate product, [Th_9], characterized by a sandwich structure. This product continues to capture mononuclear [Th] in the reaction system, ultimately leading to the formation of the [Th_{13}] cluster. A portion of the O^{2-}/OH^- coordination sites on the surface of the [Th_{13}] cluster is occupied by nickel ions, resulting in the formation of the heterometallic cluster [$Th_{13}Ni_6$]. Furthermore, under the induction of different alkali metal cations, the [$Th_{13}Ni_6$] clusters can further assemble to form 3D frameworks with various packing patterns and topological structures (IHEP-25, IHEP-26, IHEP-27, IHEP-28, and IHEP-31). Their core structure $[Th_{13}Ni_6(O)_8(OH)_{24}]^{24+}$ remains stable (Table 2). Therefore, the introduction of nickel ions plays a critical role in the formation of [Th_{13}] clusters. On the one hand, the lacuna clusters formed by the partial disassembly of [$Th_6(sba)_{12}$] clusters induced by Ni^{2+} subsequently reorganize in the solution to form [Th_{13}] clusters. On the other hand, Ni^{2+} and sba^{2-} ligands function as capping units, halting further aggregation of the clusters into polymers e.g., thorium hydroxide.

CO_2 photoreduction using IHEP-28

In recent years, solar-driven artificial carbon dioxide reduction reactions (CO_2RR) have gradually gained widespread attention for their potential to reduce greenhouse gas emissions and lower energy demand. To achieve this goal, synthesizing highly efficient and selective photocatalysts to lower the thermodynamic energy barrier has become a critical issue that needs to be addressed. Among the various photocatalysts developed for CO_2 reduction, nickel compounds are considered one of the promising candidates[73–75]. A significant advantage of these photocatalysts is that CO_2 can effectively bind to and be activated by the nickel center, thereby promoting its conversion efficiency under solar irradiation. In this work, the [$Th_{13}Ni_6$] cluster exhibits a local [$NiTh_3O_3$] structural unit, which can be regarded as a discrete molecular equivalent of the nickel-supported catalyst Ni@thoria[54,76,77] (Supplementary Fig. S21). Therefore, the [$Th_{13}Ni_6$] cluster holds promise for application in the photocatalytic reduction of CO_2. However, as mentioned previously, due to the substitutability of the surface ligands on the [$Th_{13}Ni_6$] clusters, the discrete [$Th_{13}Ni_6$] clusters (IHEP-25, IHEP-26, IHEP-27, and IHEP-31) we obtained are difficult to simultaneously meet the requirements of high purity and high yield in experimental applications, primarily because these clusters often mix with each other. Once the [$Th_{13}Ni_6$] clusters are interlinked with the $[Na_4(OH)_3(H_2O)_3]^+$ clusters to form a 2D coordination polymer (IHEP-28), both purity and yield are significantly enhanced, and this 2D structure also contributes to improving the stability of the materials. Furthermore, the porous structure of IHEP-28 can expose more active sites, thereby further enhancing its photocatalytic performance. In addition, IHEP-28 features excellent stability in both air and common solvents (Supplementary Fig. S22). Based on these factors, in the subsequent research, we will focus on IHEP-28 as our primary subject to explore the photocatalytic reduction performance of the [$Th_{13}Ni_6$] cluster for CO_2.

Photocatalytic CO_2 reduction experiments utilizing IHEP-28 as the catalyst were conducted in a CH_3CN: H_2O mixture (4:1 volume ratio), employing $[Ru(bpy)_3]Cl_2{\cdot}6H_2O$ as the photosensitizer (10 mg) without the need for an additional sacrificial agent. The CO_2RR results, presented in Fig. 4a under 1 atm of pressure and visible light irradiation ($\lambda > 420$ nm), reveal a nearly linear growth in CO production over 3 h, amounting to a rate of 112.7 $\mu mol{\cdot}h^{-1}{\cdot}g^{-1}$. The photocatalytic process displayed an exceedingly high selectivity for CO production, nearly 100%, with no other gas or liquid phase products detected (Supplementary Fig. S23a). This rate is comparable to reported Ni-based cluster or MOF photocatalysts without additional sacrificial agent (Supplementary Table S2). The CO_2 photoreduction system manifests an apparent quantum yield (AQY) of 0.74% under monochromatic light irradiation of 525 nm. Control experiments, as depicted in Fig. 4b and Supplementary Table S3, yielded a negligible amount of CO. Notably, when CO_2 was substituted with Ar, no CO production was observed, confirming that the CO is derived from CO_2 reduction rather than the decomposition of IHEP-28, which can also be confirmed by the isotopic test (Supplementary Fig. S23b). Remarkably, IHEP-28 efficiently catalyzes the photocatalytic reduction of CO_2 even in the absence of photosensitizers and sacrificial agents, achieving a CO production rate of 10.1 $\mu mol{\cdot}h^{-1}{\cdot}g^{-1}$. Post-photocatalysis, PXRD analysis confirmed that IHEP-28 retained its crystallinity, indicating its excellent chemical stability (Supplementary Fig. S24). Intriguingly, after three catalytic cycles, IHEP-28 maintained similar catalytic activity and high crystallinity, demonstrating its excellent stability during the photocatalytic process (Supplementary Fig. S25).

The band gap energy (*Eg*) of IHEP-28 is determined to be 2.43 eV, based on the UV-Vis-NIR spectrum and Tauc plots (Supplementary

Table 2 | The Formulae of Compounds IHEP-25 - IHEP-31 and Their Core Structures

Compounds	Formulae of compounds	Formulae of cores
IHEP-25	$[Th_{13}Ni_6(O)_8(OH)_{18}(OH)_6(sba)_{12}(H_2O)_{18}]$	$[Th_{13}Ni_6(O)_8(OH)_{24}]^{24+}$
IHEP-26	$[Th_{13}Ni_6(O)_8(OH)_{24}(sba)_{12}(H_2O)_{12}(CH_3CN)_6]$	$[Th_{13}Ni_6(O)_8(OH)_{24}]^{24+}$
IHEP-27	$[Th_{13}Ni_6(O)_8(OH)_{24}(sba)_{12}(H_2O)_{18}]{\cdot}[Th_{13}Ni_6(O)_8(OH)_{24}(sba)_{12}(H_2O)_{12}(CH_3CN)_6]$	$[Th_{13}Ni_6(O)_8(OH)_{24}]^{24+}$
IHEP-28	$\{[Th_{13}Ni_6(O)_8(OH)_{24}(sba)_{14}(H_2O)_{12}(CH_3COO)_2(CH_3CN)_2]_3[Na_4(OH)_3(H_2O)_3]_2\}_n$	$[Th_{13}Ni_6(O)_8(OH)_{24}]^{24+}$
IHEP-29	$Na_6[Th_6(O)_4(OH)_4(sba)_{12}(H_2O)_6]$	$[Th_6(O)_4(OH)_4]^{12+}$
IHEP-30	$[Th(sba)_2(H_2O)_3]_n{\cdot}2nH_2O$	Th^{4+}
IHEP-31	$[Th_{13}Ni_6(O)_8(OH)_{24}(sba)_{12}(H_2O)_{10}(CH_3CN)_2]{\cdot}20H_2O$	$[Th_{13}Ni_6(O)_8(OH)_{24}]^{24+}$

H_2sba: 2-sulfobenzoic acid

https://doi.org/10.1038/s41467-025-58590-z

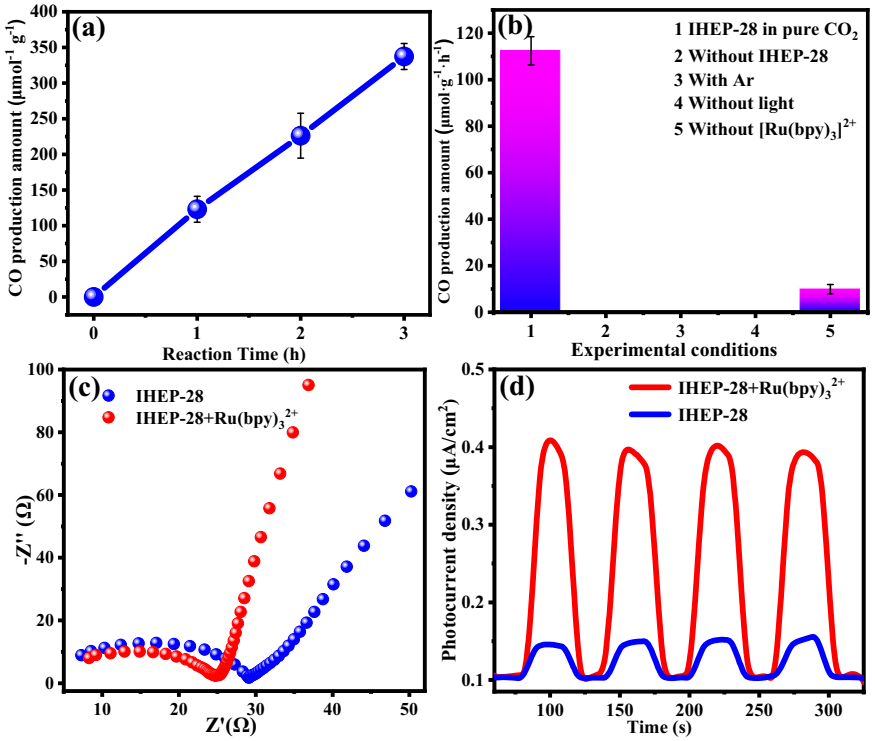

Fig. 4 | The photocatalytic CO_2 reduction performance and electrochemical characterization of IHEP-28. a Time-dependent evolution of the photocatalytic reduction of CO_2 to CO over IHEP-28. **b** CO production rates of IHEP-28 under different conditions. Conduct three parallel experiments, calculate and label the standard deviation as the error bar. **c** Electrochemical impedance spectra (EIS) taken on IHEP-28 and the IHEP-28 + $[Ru(bpy)_3]^{2+}$ mixture under visible light irradiation. **d** Transient photocurrent response (TPR) of IHEP-28 and the IHEP-28 + $[Ru(bpy)_3]^{2+}$ mixture under visible light irradiation.

Fig. S26a, b). The Mott-Schottky plots result indicates that IHEP-28 behaves as a typical n-type semiconductor, evidenced by a positive slope with the flat band potential of − 1.12 V (vs. Ag/AgCl), as shown in Supplementary Fig. S26c. Consequently, the conduction band (CB) potential of IHEP-28 is estimated to be − 0.92 V vs NHE. Therefore, the valence band (E_{VB}) of IHEP-28 is determined to be 1.51 V (vs NHE), according to the empirical formula $E_{VB} = E_{CB} + E_g$ (1) (Supplementary Fig. S26d)[78]. To confirm the products of the reaction between the photoinduced holes and H_2O, we first examined the gaseous products and did not detect the presence of oxygen. Subsequently, based on the classic Ti-oxalate method reported in the literature, we tested the solution after the photocatalytic reaction and detected the formation of H_2O_2 (Supplementary Fig. S27)[79]. Therefore, under visible light irradiation, photoinduced electrons move to catalytically active sites for CO_2 reduction while corresponding holes are consumed by H_2O with the formation of H_2O_2.

A set of electrochemical techniques were used to check the electrochemical behaviors in IHEP-28[80,81]. The electrochemical impedance spectroscopy (EIS) test was performed to investigate the interfacial charge transfer and recombination (Fig. 4c). Nyquist plots acquired under illumination conditions show that the charge transfer impedance of the IHEP-28 + $[Ru(bpy)_3]^{2+}$ mixture is smaller than that of the IHEP-28 alone, suggesting the better separated photoexcited charged pairs by introduction of $Ru(bpy)_3^{2+}$, ultimately improving the photocatalytic performance. As shown in Fig. 4d, there is a much higher transient photocurrent response signal observed on the IHEP-28 + $[Ru(bpy)_3]^{2+}$ mixture, while the absence of $Ru(bpy)_3^{2+}$ yields a much weaker photocurrent. These test results indicate that the introduction of $Ru(bpy)_3^{2+}$ significantly improved the transfer and separation efficiency of photogenerated electrons and holes in IHEP-28, which aligns with the experimental results showing that $Ru(bpy)_3^{2+}$ enhances the photocatalytic reduction efficiency of CO_2 by IHEP-28.

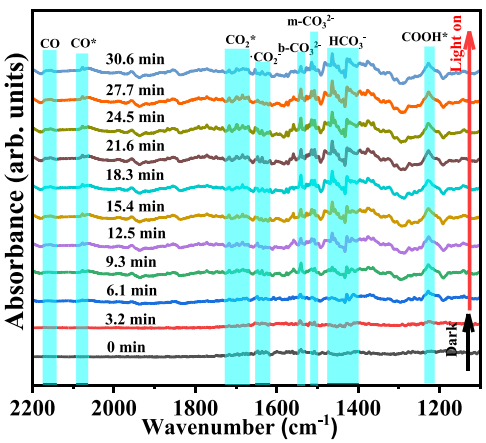

Fig. 5 | In situ DRIFTS characterization. In situ DRIFTS spectra for detecting the reaction intermediates in photocatalytic CO_2 reduction over IHEP-28 under visible light irradiation.

Mechanism of photocatalytic CO_2 reduction

By employing in situ diffuse reflectance infrared Fourier transform spectroscopy (DRIFTS), it is possible to monitor in real-time the surface species adsorbed during the CO_2RR process and the intermediates generated from CO_2 conversion. As shown in Fig. 5, the time-resolved spectra of IHEP-28, after introducing moist CO_2 in the dark, reveal characteristic infrared peaks of the active $•CO_2^-$ intermediate (1632 cm^{-1}), bidentate carbonate (b-CO_3^{2-}, 1540 cm^{-1}), monodentate carbonate (m-CO_3^{2-}, 1514 cm^{-1})[82]. Under light irradiation, several characteristic infrared peaks can be observed around 1698 cm^{-1}, indicating the generation of $*CO_2$, which is attributed to the activation of adsorbed CO_2 by photogenerated electron[83]. Meanwhile, new peaks at 1226

https://doi.org/10.1038/s41467-025-58590-z

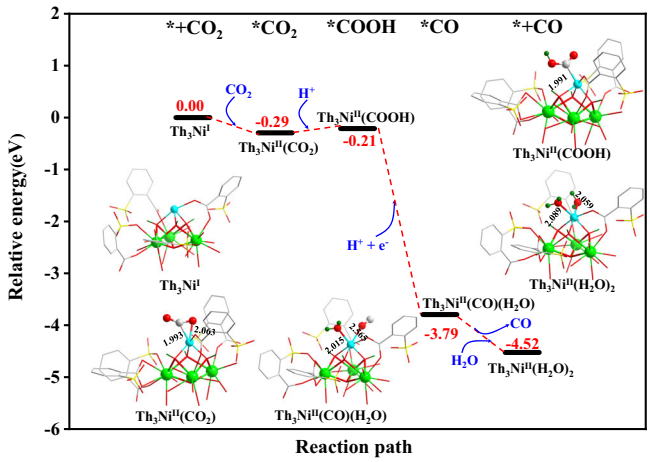

Fig. 6 | Computational studies on the reaction pathway. Potential energy profile for the possible mechanism of CO_2 activation by IHEP-28. Color scheme: Th, green; Ni, cyan; C, gray; O, red; S, yellow; H, dark green.

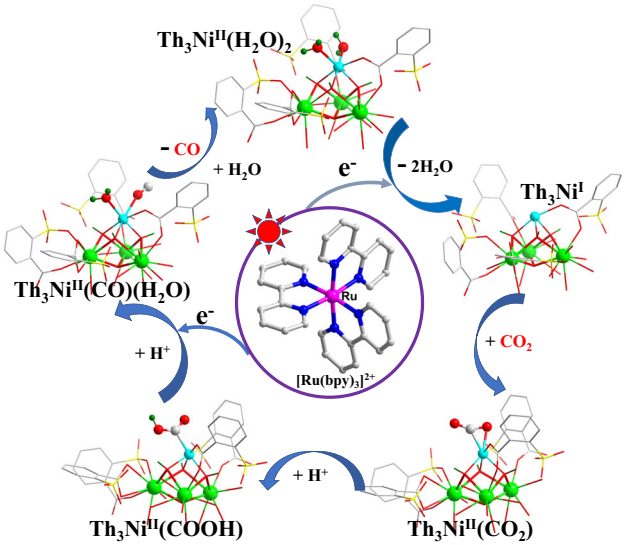

Fig. 7 | Schematic mechanism of the photocatalytic CO_2 reduction by IHEP-28. The CO_2 molecules absorbed on the IHEP-28 surface were reduced into CO undergo a two-electron process under visible light irradiation. Color scheme: Th, green; Ni, cyan; C, gray; O, red; S, yellow; H, dark green; Ru, pink.

and 1558 cm^{-1} can also be observed, and their peak intensities increase as time go on. Both peaks should be assigned to the COOH* group, which is a key intermediate during CO_2 photoreduction into CO[84]. In addition, the detection of the CO* absorption band at 2077 cm^{-1} and the gas CO absorption band around 2162 cm^{-1} further confirms the formation of CO. Moreover, the CO_2RR process detects the formation of HCO_3^- (1426 and 1462 cm^{-1})[85].

DFT calculations were conducted to further elucidate the CO_2RR mechanism of IHEP-28. As shown in Supplementary Fig. S28, considering the similar coordination mode of Ni^{2+} ions in IHEP-28, we extracted the $Th_3Ni^{II}(H_2O)_2$ structural unit from the $Th_{13}Ni_6$ cluster as a model for DFT calculations. In this model structure, the Th_3 unit bridged by three hydroxyl groups serves as the support for the catalytically active center Ni^{2+}. Under the excitation of visible light, $Th_3Ni^{II}(H_2O)_2$ enriched a photogenerated electron from the photosensitizer while simultaneously losing two coordinated water molecules, thereby forming Th_3Ni^{I} with unsaturated coordination. As shown in Fig. 6, the Th_3Ni^{I} unite combines with a CO_2 molecule to form the intermediate complex $Th_3Ni^{II}(CO_2)$, accompanied by an exothermic process of − 0.29 eV, which indicates that this reaction is thermodynamically feasible. In the $Th_3Ni^{II}(CO_2)$ complex, the CO_2 molecule is coordinated to the Ni atom with the η^2(C, O) coordination mode, where the Ni-C and Ni-O bond distance is 1.993 and 2.063 Å, respectively. The reaction from $Th_3Ni^{II}(CO_2)$ to $Th_3Ni^{II}(COOH)$ is endothermic by 0.08 eV. In this process, an O-H bond was formed in the $Th_3Ni^{II}(COOH)$ complex, resulting in a change in the coordination mode between the Ni atom and CO_2 molecule from η^2(C, O) to η^1(C), with the Ni-C bond distance of 1.991 Å. Subsequently, the $Th_3Ni^{II}(COOH)$ complex captured an additional photogenerated electron from the photosensitizer while simultaneously acquiring a proton (H^+) to form the intermediate complex $Th_3Ni^{II}(CO)(H_2O)$. This process was accompanied by a significant exothermic release of − 3.58 eV. In the transformation of $Th_3Ni^{II}(COOH)$ to $Th_3Ni^{II}(CO)(H_2O)$, one C = O bond of the CO_2 molecule is broken, resulting in the formation of a coordinated H_2O molecule and a coordinated CO molecule. In the $Th_3Ni^{II}(CO)(H_2O)$ complex, the bond lengths are 2.015 Å for the Ni-O_{water} bond and 2.565 Å for the Ni-$O_{C=O}$ bond. The elongated Ni-$O_{C=O}$ bond distance facilitates cleavage in the presence of water molecule, ultimately resulting in the formation of the $Th_3Ni^{II}(H_2O)_2$ complex while concurrently releasing a CO molecule, through an exothermic process with the energy release of − 0.73 eV.

Based on previous related reports[86,87], the aforesaid in situ IR analysis, and the DFT calculations, the photocatalytic CO_2RR mechanism of IHEP-28 is proposed as follows. Under visible light irradiation, electrons photoinduced by the photosensitizer $[Ru(bpy)_3]^{2+}$ transferred to the $Th_{13}Ni_6$ cluster of IHEP-28, and then the CO_2 molecules absorbed on IHEP-28 surface were reduced into CO undergo a two-electron process (Fig. 7).

Discussion

In summary, the mixed-metal cluster $[Th_{13}Ni_6O_8(OH)_{24}(H_2O)_{18}(sba)_{12}]$ (IHEP-25) was synthesized using a competitive metal ion approach. The cluster features a classical α-Keggin type $[Th_{13}O_8(OH)_{24}]$ core, marking a new hydrolytic species of Th(IV). DFT calculations indicate that the HOMO-LUMO gaps for the $[Th_{13}(O)_8(OH)_{24}]^{12+}$ core structure and the $[Th_{13}(O)_8(OH)_{24}Ni_6(H_2O)_{18}(sba)_{12}]$ cluster are 4.03 eV and 2.61 eV, respectively, suggesting exceptional stability of the heterometallic cluster. Modifications to the reaction conditions allow for the substitution of some coordinated H_2O molecules in IHEP-25 with CH_3CN, yielding three new $[Th_{13}Ni_6]$ clusters: $[Th_{13}Ni_6(O)_8(OH)_{24}(sba)_{12}(H_2O)_{12}(CH_3CN)_6]$ (IHEP-26), $[Th_{13}Ni_6(O)_8(OH)_{24}(sba)_{12}(H_2O)_{18}][Th_{13}Ni_6(O)_8(OH)_{24}(sba)_{12}(H_2O)_{12}(CH_3CN)_6]$ (IHEP-27) and $[Th_{13}Ni_6(O)_8(OH)_{24}(sba)_{12}(H_2O)_{10}(CH_3CN)_2]$ (IHEP-31), which further attest to the high stability of the $[Th_{13}Ni_6]$ cluster. In addition, the $[Th_{13}Ni_6]$ cluster can be interconnected with the cationic cluster $[Na_4(OH)_3(H_2O)_3]^+$ to construct a 2D honeycomb framework $\{[Th_{13}Ni_6(O)_8(OH)_{24}(sba)_{14}(H_2O)_{12}(CH_3COO)_2(CH_3CN)_2]_3[Na_4(OH)_3(H_2O)_3]_2\}_n$ (IHEP-28). Without the need for additional sacrificial agents, IHEP-28 demonstrates remarkable activity in the visible-light-driven photocatalytic reduction of CO_2, achieving CO production rates of 10.1 $\mu mol \cdot h^{-1} \cdot g^{-1}$ (without a photosensitizer) and 112.7 $\mu mol \cdot h^{-1} \cdot g^{-1}$ (with $[Ru(bpy)_3]^{2+}$ as a photosensitizer), respectively. The mechanism of photocatalytic CO_2 reduction by IHEP-28 was clearly elaborated using in situ DRIFTS and theoretical calculations. This work suggests that under complex environmental conditions, actinide metal ions may exist as mixed-metal clusters. The presence of heterometallic ions can alter the hydrolysis patterns of actinide metal ions, leading to the formation of new hydrolytic species and influencing the behavior and migration of radionuclides in the environment.

Methods

Materials availability

Caution! Thorium nitrate ($Th(NO_3)_4 \cdot 4H_2O$, 98%, Aladdin) is radioactive and chemically toxic; precautions with suitable care and protection for

handling such substances must be followed. $Ni(NO_3)_2$•$6H_2O$ (98%, Xilong Chemical Industry Incorporated Co. LTD), thiosalicylic acid (99%, Aladdin), $[Ru(bpy)_3]Cl_2$·$6H_2O$ (98%, Aladdin), LiOH•H_2O (98%, Energy Chemical), NaOH (99%, Innochem), KOH (95%, Shanghai Titan Scientific Co., Ltd), CH_3CN (99%, Shanghai Titan Scientific Co., Ltd) and other reagents were analytical grade and used without further purification.

Synthesis of IHEP-25 $[Th_{13}Ni_6(O)_8(OH)_{24}(sba)_{12}(H_2O)_{18}]$

$Th(NO_3)_4$ (0.5 M, 200 μL), $Ni(NO_3)_2$ (0.5 M, 200 μL), thiosalicylic acid (0.4 mmol), CH_3CN (3 mL), KOH (1 M, 75 μL) were loaded into a 25 mL autoclave. The autoclave was sealed, heated to 150 °C in an oven for 12 h, and then cooled to ambient temperature. A small quantity of almost colorless square block crystals of IHEP-25 could be obtained, as well as a lot of amorphous solids.

Synthesis of IHEP-26 $[Th_{13}Ni_6(O)_8(OH)_{24}(sba)_{12}(H_2O)_{12}(CH_3CN)_6]$

$Th(NO_3)_4$ (0.5 M, 200 μL), $Ni(NO_3)_2$ (0.5 M, 200 μL), thiosalicylic acid (0.4 mmol), CH_3CN (3 mL), KOH (1 M, 125 μL) were loaded into a 25 mL autoclave. The autoclave was sealed, heated to 150 °C in an oven for 12 h, and then cooled to ambient temperature. Almost colorless rhomboid crystals of IHEP-26 could be obtained, as well as a lot of amorphous solids.

Synthesis of IHEP-27 $[Th_{13}Ni_6(O)_8(OH)_{24}(sba)_{12}(H_2O)_{18}]$ •$[Th_{13}Ni_6(O)_8(OH)_{24}(sba)_{12}(H_2O)_{12}(CH_3CN)_6]$

$Th(NO_3)_4$ (0.5 M, 200 μL), $Ni(NO_3)_2$ (0.5 M, 200 μL), thiosalicylic acid (0.4 mmol), CH_3CN (3 mL), NaOH (1 M, 210 μL) were loaded into a 25 mL autoclave. The autoclave was sealed, heated to 150 °C in an oven for 12 h, and then cooled to ambient temperature. A small quantity of light green polygonal crystal crystals of IHEP-27 could be obtained, as well as a lot of green square block crystals of IHEP-28 and amorphous solids.

Synthesis of IHEP-28 $\{[Th_{13}Ni_6(O)_8(OH)_{24}(sba)_{14}(H_2O)_{12}(CH_3COO)_2(CH_3CN)_2]_3[Na_4(OH)_3(H_2O)_3]_2\}_n$

$Th(NO_3)_4$ (0.5 M, 200 μL), $Ni(NO_3)_2$ (0.5 M, 200 μL), thiosalicylic acid (0.4 mmol), CH_3CN (3 mL), NaOH (1 M, 270 μL) were loaded into a 25 mL autoclave. The autoclave was sealed, heated to 150 °C in an oven for 12 h, and then cooled to ambient temperature. The green square block crystals of IHEP-28 were produced and washed three times with fresh CH_3OH.

Synthesis of IHEP-29 $Na_6[Th_6(O)_4(OH)_4(sba)_{12}(H_2O)_6]$

$Th(NO_3)_4$ (0.5 M, 200 μL), thiosalicylic acid (0.2 mmol), CH_3CN (3 mL), NaOH (1 M, 185 μL) were loaded into a 25 mL autoclave. The autoclave was sealed, heated to 150 °C in an oven for 12 h, and then cooled to ambient temperature. The colorless fusiform crystals of IHEP-29 were produced, as well as a small quantity of big block crystals of IHEP-30.

Synthesis of IHEP-30 $[Th(sba)_2(H_2O)_3]_n$•$2nH_2O$

$Th(NO_3)_4$ (0.5 M, 200 μL), thiosalicylic acid (0.2 mmol), CH_3CN (3 mL), NaOH (1 M, 120 μL) were loaded into a 25 mL autoclave. The autoclave was sealed, heated to 150 °C in an oven for 12 h, and then cooled to ambient temperature. The block crystals of IHEP-30 were produced.

Synthesis of IHEP-31 $[Th_{13}Ni_6(O)_8(OH)_{24}(sba)_{12}(H_2O)_{10}(CH_3CN)_2]$•$20H_2O$

$Th(NO_3)_4$ (0.5 M, 200 μL), $Ni(NO_3)_2$ (0.5 M, 200 μL), thiosalicylic acid (0.4 mmol), CH_3CN (3 mL), LiOH (1 M, 270 μL) were loaded into a 25 mL autoclave. The autoclave was sealed, heated to 150 °C in an oven for 12 h, and then cooled to ambient temperature. The yellow-green block crystals of IHEP-31 were produced and washed three times with fresh CH_3OH.

Physical properties

IR measurements were obtained on a Bruker Tensor 27 infrared spectrometer. The sample was diluted with spectroscopic KBr and pressed into a pellet. The measured wavenumber is between 400 and 4000 cm^{-1}. Powder X-ray diffraction measurements were made using a Bruker D8 Advance diffractometer with Cu Kα radiation (λ = 1.5406 Å) in the range 5-50° (step size: 0.02°). Thermogravimetric analysis (TGA) was performed on a TA Q500 analyzer over the temperature range of 30–800 °C in an air atmosphere with a heating rate of 5 °C•min^{-1}. The in situ diffuse reflectance infrared Fourier transform spectroscopy (DRIFTS) was conducted on a Nicolet iS 50 (Thermo Fisher Scientific, USA) FT-IR spectrometer. The UV-vis diffuse-reflectance spectroscopy (UV-vis DRS) were obtained on a UV-visible spectrophotometer (HITACHI UH4150), and $BaSO_4$ was used as a reference. The photocurrent responses, Mott-Schottky plots, and the electrochemical impedance spectroscopy (EIS) were measured at an electrochemical workstation (PGSTAT302N Autolab, Metrohm). Normally, the Ag/AgCl electrode as the reference electrode, the platinum sheet electrode as the counter electrode, and the glassy carbon electrode as the working electrode formed a three-electrode system with 0.1 M sodium sulfate as the electrolyte. In the test of photocurrent responses, the F-doped tin oxide (FTO) conductive glass electrode was selected as the working electrode.

Photocatalytic performance measurements

The photocatalyst (15 mg) and photosensitizer $[Ru(bpy)_3]Cl_2$·$6H_2O$ (10 mg) was added to 4 mL of acetonitrile and 1 mL H_2O in a custom-made 20 mL photocatalytic reaction cell, which was degassed and saturated with ultra-pure CO_2 before sealing. The photocatalytic reactions were carried out under irradiation of a 300 W Xe lamp (CEL-PE300L-3A) equipped with a 420 nm filter. After the reaction, potential gaseous products (H_2, CO, CH_4) were determined by gas chromatography (GC, 8890, Agilent Technologies, Inc.). Potential liquid products were determined by ^1H NMR spectra using 500 μL of the liquid after reaction mixed with 100 μL of D_2O and 0.05 μL dimethyl sulfoxide as internal standard. In the isotope labeling experiment, $^{13}CO_2$ was used as the reactant to analyze the carbon source of photocatalytic CO_2 reduction to produce CO. The ^{13}CO was analyzed by gas chromatography-mass spectrometry (7890B, Agilent Technologies).

Data availability

The authors declare that the data supporting the findings of this study are provided in the article/Supplementary Information/Source Data file. All data are available from the corresponding author upon request. The X-ray crystallographic coordinates for structures reported in this study have been deposited at the Cambridge Crystallographic Data Center (CCDC), under deposition numbers 2324079-2324084 and 2412223. These data can be obtained free of charge from The Cambridge Crystallographic Data Center via www.ccdc.cam.ac.uk/data_request/cif. Source data are provided in this paper.

References

1. Zheng, X. Y. et al. A gigantic molecular wheel of $\{Gd_{140}\}$: A new member of the molecular wheel family. *J. Am. Chem. Soc.* **139**, 18178–18181 (2017).
2. Kang, X. M. et al. An ultrastable matryoshka $[Hf_{13}]$ nanocluster as a luminescent sensor for concentrated Alkali and Acid. *Angew. Chem. Int. Edit.* **58**, 16610–16616 (2019).
3. Hu, F., Li, J. J., Guan, Z. J., Yuan, S. F. & Wang, Q. M. Formation of an Alkynyl-protected Ag_{112} Silver nanocluster as promoted by chloride released in situ from CH_2Cl_2. *Angew. Chem. Int. Edit.* **59**, 5312–5315 (2020).
4. Romanelli, M., Kumar, G. A., Emge, T. J., Riman, R. E. & Brennan, J. G. Intense near-IR emission from nanoscale lanthanoid fluoride clusters. *Angew. Chem. Int. Ed.* **47**, 6049–6051 (2008).

5. Zheng, X. Y., Xie, J., Kong, X. J., Long, L. S. & Zheng, L. S. Recent advances in the assembly of high-nuclearity lanthanide clusters. *Coord. Chem. Rev.* **378**, 222–236 (2019).
6. Huang, R. W. et al. $Cu_{81}(PhS)_{46}(^tBuNH_2)_{10}(H)_{32}]^{3+}$ Reveals the coexistence of large planar cores and hemispherical shells in high-nuclearity copper nanoclusters. *J. Am. Chem. Soc.* **142**, 8696–8705 (2020).
7. Bhattacharya, S. et al. Discovery and supramolecular interactions of neutral palladium-oxo clusters Pd_{16} and Pd_{24}. *Angew. Chem. Int. Edit.* **60**, 3632–3639 (2021).
8. Achenbach, B. et al. Porous salts containing Cationic Al_{24}-hydroxide-acetate clusters from scalable, green and aqueous synthesis routes. *Angew. Chem. Int. Edit.* **62**, e202218679 (2023).
9. Luo, X. M., Li, Y. K., Dong, X. Y. & Zang, S. Q. Platonic and Archimedean solids in discrete metal-containing clusters. *Chem. Soc. Rev.* **52**, 383–444 (2023).
10. Zhang, Y. J., de Azambuja, F. & Parac-Vogt, T. N. The forgotten chemistry of group(IV) metals: A survey on the synthesis, structure, and properties of discrete Zr(IV), Hf(IV), and Ti(IV) oxo clusters. *Coord. Chem. Rev.* **438**, 213886 (2021).
11. Zhu, C. et al. Fluorescence or phosphorescence? The metallic composition of the nanocluster kernel does matter. *Angew. Chem. Int. Edit.* **61**, e202205947 (2022).
12. Dong, G. et al. Multi-layer 3D chirality and double-helical assembly in a copper nanocluster with a triple-helical Cu_{15} core. *Angew. Chem. Int. Edit.* **62**, e202302595 (2023).
13. Zheng, Z. & Burns, P. C. *Recent Development in Clusters of Rare Earths and Actinides: Chemistry and Materials*. **173**, (Springer, 2017).
14. Thomas, F. & Neck, V. Aquatic chemistry and solubility phenomena of actinide oxides/hydroxides. *Pure Appl. Chem.* **74**, 1895–1907 (2002).
15. Novikov, A. P. et al. Colloid transport of plutonium in the far-field of the mayak production association. *Russia. Science.* **314**, 638 (2006).
16. Kersting, A. B. et al. Migration of plutonium in ground water at the Nevada Test Site. *Nature* **397**, 56–59 (1999).
17. Chatelain, L., Faizova, R., Fadaei-Tirani, F., Pécaut, J. & Mazzanti, M. Structural snapshots of cluster growth from $\{U_6\}$ to $\{U_{38}\}$ during the hydrolysis of UCl_4. *Angew. Chem. Int. Edit.* **58**, 3021–3026 (2019).
18. Sigmon, G. E. et al. Uranyl-peroxide interactions favor nanocluster self-assembly. *J. Am. Chem. Soc.* **131**, 16648–16649 (2009).
19. Vlaisavljevich, B., Gagliardi, L. & Burns, P. C. Understanding the structure and formation of Uranyl peroxide nanoclusters by quantum chemical calculations. *J. Am. Chem. Soc.* **132**, 14503–14508 (2010).
20. Falaise, C., Hickam, S. M., Burns, P. C. & Nyman, M. From aqueous speciation to supramolecular assembly in alkaline earth-uranyl polyoxometalates. *Chem. Commun.* **53**, 9550–9553 (2017).
21. Hu, S. X., Zhang, P., Lu, E. L. & Zhang, P. Decisive role of 5f-orbital covalence in the structure and stability of pentavalent transuranic Oxo $[M_6O_8]$ clusters. *Inorg. Chem.* **59**, 18068–18077 (2020).
22. Natrajan, L. S., Swinburne, A. N., Andrews, M. B., Randall, S. & Heath, S. L. Redox and environmentally relevant aspects of actinide(IV) coordination chemistry. *Coord. Chem. Rev.* **266**, 171–193 (2014).
23. Knope, K. E. & Soderholm, L. Solution and solid-state structural chemistry of actinide hydrates and their hydrolysis and condensation products. *Chem. Rev.* **113**, 944–994 (2013).
24. Qiu, J. & Burns, P. C. Clusters of actinides with Oxide, Peroxide, or Hydroxide bridges. *Chem. Rev.* **113**, 1097–1120 (2013).
25. Silver, M. A. & Albrecht-Schmitt, T. E. Evaluation of f-element borate chemistry. *Coord. Chem. Rev.* **323**, 36–51 (2016).
26. Zhang, M. X. et al. Intrinsic semiconducting behavior in a large mixed-valent Uranium(V/VI) cluster. *Angew. Chem. Int. Ed.* **60**, 9886–9890 (2021).
27. Soderholm, L., Almond, P. M., Skanthakumar, S., Wilson, R. E. & Burns, P. C. The structure of the plutonium oxide nanocluster $[Pu_{38}O_{56}Cl_{54}(H_2O)_8]^{14-}$. *Angew. Chem. Int. Edit.* **47**, 298–302 (2008).
28. Wilson, R. E., Skanthakumar, S. & Soderholm, L. Separation of Plutonium Oxide nanoparticles and colloids. *Angew. Chem. Int. Ed.* **50**, 11234–11237 (2011).
29. Martin, N. P. et al. $\{Np_{38}\}$ clusters: the missing link in the largest poly-oxo cluster series of tetravalent actinides. *Chem. Commun.* **54**, 10060–10063 (2018).
30. Cooper, N., Minakata, D., Begovic, M. & Crittenden, J. Should we consider using liquid fluoride Thorium reactors for power generation? *Environ. Sci. Technol* **45**, 6237–6238 (2011).
31. Hargraves, R. & Moir, R. J. A. S. Liquid fluoride Thorium reactors: An old idea in nuclear power gets reexamined. **98**, 304-313 (2010).
32. Serp, J. et al. The molten salt reactor (MSR) in generation IV: Overview and perspectives. *Prog. Nucl. Energ.* **77**, 308–319 (2014).
33. Andreo, J. et al. Autoluminescent metal-organic frameworks (MOFs): Self-photoemission of a highly stable Thorium MOF. *J. Am. Chem. Soc.* **140**, 14144–14149 (2018).
34. Gilson, S. E. et al. Unprecedented radiation resistant Thorium-Binaphthol metal-organic framework. *J. Am. Chem. Soc.* **142**, 13299–13304 (2020).
35. Chen, R. H. et al. Molecular Thorium Trihydrido Clusters stabilized by cyclopentadienyl ligands. *Angew. Chem. Int. Ed.* **59**, 11250–11255 (2020).
36. Li, Y. et al. A mesoporous cationic thorium-organic framework that rapidly traps anionic persistent organic pollutants. *Nat. Commun.* **8**, 1354 (2017).
37. Xu, H. et al. High uptake of ReO_4^- and CO_2 conversion by a radiation-resistant Thorium-Nickle $[Th_{48}Ni_6]$ nanocage-based metal-organic framework. *Angew. Chem. Int. Edit.* **58**, 6022–6027 (2019).
38. Woidy, P. & Kraus, F. $Th_{10}(\mu\text{-}F_{16})(\mu_3\text{-}O_4)(\mu_4\text{-}O_4)(NH_3)_{32}](NO_3)_8 \cdot 19.6\ NH_3$ - the Largest Thorium complex from solution known to date. *Z. Anorg. Allg. Chem.* **640**, 1547–1550 (2014).
39. Yin, M. et al. A $[Th_8Co_8]$ Nanocage-based metal–organic framework with extremely narrow window but flexible nature enabling dual-sieving effect for both isotope and isomer separation. *CCS Chem.* **4**, 1016–1027 (2022).
40. Lu, H. et al. A new concept of radiation detection based on a fluorochromic and piezochromic nanocluster. *J. Am. Chem. Soc.* **144**, 3449–3457 (2022).
41. Wang, Y. et al. Employing an unsaturated Th^{4+} site in a porous Thorium–Organic framework for Kr/Xe uptake and separation. *Angew. Chem., Int. Ed.* **57**, 5783–5787 (2018).
42. Tsantis, S. T. et al. Pentanuclear Thorium(IV) coordination cluster from the use of Di(2-pyridyl) ketone. *Inorg. Chem.* **60**, 11888–11892 (2021).
43. Wilson, R. E., Skanthakumar, S., Sigmon, G., Burns, P. C. & Soderholm, L. Structures of dimeric hydrolysis products of thorium. *Inorg. Chem.* **46**, 2368–2372 (2007).
44. Wacker, J. N. et al. Monomeric and trimeric Thorium chlorides isolated from acidic aqueous solution. *Inorg. Chem.* **58**, 10871–10882 (2019).
45. Travia, N. E., Scott, B. L. & Kiplinger, J. L. A rare tetranuclear Thorium(IV) μ_4-Oxo cluster and dinuclear Thorium(IV) complex assembled by carbon-oxygen bond activation of 1,2-Dimethoxyethane (DME). *Chem. Eur. J.* **20**, 16846–16852 (2014).
46. Tsantis, S. T. et al. Tetranuclear oxido-bridged thorium(iv) clusters obtained using tridentate Schiff bases. *Dalton. Trans.* **48**, 15668–15678 (2019).
47. Takao, S. et al. First hexanuclear U^{IV} and Th^{IV} formate complexes - structure and stability range in aqueous solution. *Eur. J. Inorg. Chem.* **2009**, 4771–4775 (2009).
48. Hu, Y. J., Knope, K. E., Skanthakumar, S. & Soderholm, L. Understanding the Ligand-directed assembly of a hexanuclear Th^{IV} molecular cluster in aqueous solution. *Eur. J. Inorg. Chem.* **2013**, 4159–4163 (2013).

49. Vanagas, N. A. et al. Solution and solid state structural chemistry of Th(IV) and U(IV) 4-hydroxybenzoates. *Inorg. Chem.* **57**, 7259–7269 (2018).
50. Lin, J., Jin, G. B. & Soderholm, L. $Th_3[Th_6(OH)_4O_4(H_2O)_6](SO_4)(H_2O)_{13}$: A self-assembled microporous open-framework thorium sulfate. *Inorg. Chem.* **55**, 10098–10101 (2016).
51. Qian, X. Y., Zhou, T. H. & Mao, J. G. New thorium(IV)-arsonates with a $[Th_8O_{13}]^{6+}$ octanuclear core. *Dalton Trans* **44**, 13573–13580 (2015).
52. Galley, S. S., Van Alstine, C. E., Maron, L. & Albrecht-Schmitt, T. E. Understanding the scarcity of thorium peroxide clusters. *Inorg. Chem.* **56**, 12692–12694 (2017).
53. Diwu, J., Wang, S. & Albrecht-Schmitt, T. E. Periodic trends in hexanuclear actinide clusters. *Inorg. Chem.* **51**, 4088–4093 (2012).
54. Bhattacharya, S. et al. Discrete, cationic palladium(II)-Oxo clusters via f-metal ion incorporation and their macrocyclic host-guest interactions with sulfonatocalixarenes. *Angew. Chem. Int. Ed.* **61**, e202203114 (2022).
55. Kong, X. H. et al. Silver ion-induced formation of unprecedented thorium nonamer clusters via Lacuna-construction strategy. *CCS Chem.* **5**, 1144–1153 (2023).
56. Fairley, M., Unruh, D. K., Donovan, A., Abeysinghe, S. & Forbes, T. Z. Synthesis and characterization of homo- and heteronuclear molecular Al^{3+} and Th^{4+} species chelated by the ethylenediaminetetraacetate (edta) ligand. *Dalton Trans.* **42**, 13706–13714 (2013).
57. Leng, J. D. et al. Chromium chains as polydentate fluoride ligands for actinides and group IV metalst. *Dalton T* **47**, 6361–6369 (2018).
58. Duval, S. et al. Stabilization of Tetravalent 4f (Ce), 5d (Hf), or 5f (Th, U) Clusters by the [α-SiW9O34]10- Polyoxometalate. *Inorg. Chem.* **54**, 8271–8280 (2015).
59. Mishra, A., Abboud, K. A. & Christou, G. Largest mixed transition metal/actinide cluster: A bimetallic Mn/Th complex with a $[Mn_{10}Th_6O_{22}(OH)_2]^{18+}$ core. *Inorg. Chem.* **45**, 2364–2366 (2006).
60. Mishra, A., Tasiopoulos, A. J., Wernsdorfer, W., Abboud, K. A. & Christou, G. High-nuclearity Ce/Mn and Th/Mn cluster chemistry: Preparation of complexes with $[Ce_4Mn_{10}O_{10}(OMe)_6]^{18+}$ and $[Th_6Mn_{10}O_{22}(OH)_2]^{18+}$ cores. *Inorg. Chem.* **46**, 3105–3115 (2007).
61. Unruh, D. K. et al. Interplay of condensation and chelation in binary and ternary Th(IV) systems. *Inorg. Chem.* **54**, 1395–1404 (2015).
62. Niu, Q. et al. Achieving high photo/thermocatalytic product selectivity and conversion via Thorium clusters with switchable functional ligands. *J. Am. Chem. Soc.* **144**, 18586–18594 (2022).
63. Li, J., Li, X., Zhai, H. J. & Wang, L. S. Au_{20}: A tetrahedral cluster. *Science* **299**, 864–867 (2003).
64. Wang, X. B., Ding, C. F. & Wang, L. S. High resolution photoelectron spectroscopy of C_{60}-. *J. Chem. Phys.* **110**, 8217–8220 (1999).
65. Wang, X. J. et al. Heterometallic Ce^{IV}/ V^{V} Oxo clusters with adjustable catalytic reactivities. *J. Am. Chem. Soc.* **143**, 21056–21065 (2021).
66. Andrews, M. B. & Cahill, C. L. In situ oxalate formation during hydrothermal synthesis of uranyl hybrid materials. *Crystengcomm* **13**, 7068–7078 (2011).
67. Andrews, M. B. & Cahill, C. L. Uranyl hybrid material derived from in situ ligand synthesis: Formation, structure, and an unusual phase transformation. *Angew. Chem. Int. Ed.* **51**, 6631–6634 (2012).
68. Zhong, J. C., Wan, F., Sun, Y. Q. & Chen, Y. P. Luminescent hybrid lanthanide sulfates and lanthanide sulfonate-carboxylates with 1,10-phenanthroline involving oxidation of 2-mercaptonbenzoic acid. *J. Solid State Chem.* **221**, 14–20 (2015).
69. Fanning, J. C. The chemical reduction of nitrate in aqueous solution. *Coord. Chem. Rev.* **199**, 159–179 (2000).
70. Takao, S. et al. First hexanuclear U-IV and Th-IV formate complexes - structure and stability range in aqueous solution. *Eur. J. Inogr. Chem.* **2009**, 4771–4775 (2009).
71. Hu, Y.-J., Knope, K. E., Skanthakumar, S. & Soderholm, L. Understanding the ligand-directed assembly of a hexanuclear Th-IV molecular cluster in aqueous solution. *Eur. J. Inogr. Chem.* **2013**, 4159–4163 (2013).
72. Knope, K. E., Wilson, R. E., Vasiliu, M., Dixon, D. A. & Soderholm, L. Thorium(IV) molecular clusters with a hexanuclear Th core. *Inorg. Chem.* **50**, 9696–9704 (2011).
73. Yan, Z. H. et al. Encapsulating a Ni(II) molecular catalyst in photoactive metal-organic framework for highly efficient photoreduction of CO. *Sci. Bull.* **64**, 976–985 (2019).
74. Hong, D. C., Tsukakoshi, Y., Kotani, H., Ishizuka, T. & Kojima, T. Visible-light-driven photocatalytic CO reduction by a Ni(II) complex bearing a bioinspired tetradentate ligand for selective CO production. *J. Am. Chem. Soc.* **139**, 6538–6541 (2017).
75. Chen, W. P. et al. The gigantic {NiGd} hexagon: A sulfate-templated "Star-of-David" for photocatalytic CO reduction and magnetic cooling. *J. Am. Chem. Soc.* **142**, 4663–4670 (2020).
76. Mitchell, B. S. et al. Metal-support interactions in molecular single-site cluster catalysts. *J. Am. Chem. Soc.* **144**, 18459–18469 (2022).
77. Du, Y. X., Sheng, H. T., Astruc, D. & Zhu, M. Z. Atomically precise noble metal nanoclusters as efficient catalysts: A bridge between structure and properties. *Chem. Rev.* **120**, 526–622 (2020).
78. Zhang, G. P. et al. Hierarchical *Z*-scheme g-C_3N_4/Au/$ZnIn_2S_4$ photocatalyst for highly enhanced visible-light photocatalytic nitric oxide removal and carbon dioxide conversion. *Environ. Sci. Nano* **7**, 676–687 (2020).
79. Chen, Z. H. & Pignatello, J. J. Analytical methods for selectively determining hydrogen peroxide, peroxymonosulfate and peroxydisulfate in their binary mixtures. *Water Res.* **253**, 121256 (2024).
80. Zhao, S. L. et al. Ultrathin metal-organic framework nanosheets for electrocatalytic oxygen evolution. *Nat. Energy* **1**, 1–10 (2016).
81. Qin, M. F. et al. Chemically exfoliated semiconducting bimetallic porphyrinylphosphonate metal-organic layers for photocatalytic CO reduction under visible lLight. *Acs Appl. Energ. Mater.* **4**, 4319–4326 (2021).
82. Zhou, M. et al. Photocatalytic CO_2 reduction using La-Ni bimetallic sites within a covalent organic framework. *Nat. Commun.* **14**, 2473 (2023).
83. Sheng, J. P. et al. Identification of halogen-associated active sites on bismuth-based perovskite quantum dots for efficient and selective CO2-to-COphotoreduction. *Acs Nano* **14**, 13103–13114 (2020).
84. Zu, X. L. et al. Reversible switching Cu^{II}/Cu^{I} single sites catalyze high-rate and selective CO_2 photoreduction. *Angew. Chem. Int. Edit.* **62**, e202215247 (2023).
85. Yang, P. J. et al. Cobalt nitride anchored on nitrogen-rich carbons for efficient carbon dioxide reduction with visible light. *Appl. Catal. B: Environ.* **280**, 119454 (2021).
86. Chang, Q. et al. Metal-organic cages with $\{SiW_9Ni_4\}$ polyoxotungstatenodes. *Angew. Chem. Int. Edit.* **61**, e202117637 (2022).
87. Yan, Z. H. et al. Encapsulating a Ni(II) molecular catalyst in photoactive metal-organic framework for highly efficient photoreduction of CO_2. *Sci. Bull.* **64**, 976–985 (2019).

Acknowledgements

We acknowledge the support of the National Natural Science Foundation of China (22076187, K.Q.H.; 22122609, L.M.). We also thank The National Science Fund for Distinguished Young Scholars (21925603, W.Q.S.).

Author contributions

K.Q.H. and W.Q.S. conceived the idea and wrote the manuscript. Q.Y. Wu. and X.B.L. performed the theoretical calculations. W.Q.S. and L.M. reviewed and edited the manuscript. Z.W.H., J.X.W., J.D.W., and Z.H.Z. (Zhi-Heng Zhou) initiated and conducted single crystal synthesis of clusters and the photocatalytic CO_2 reduction studies, and assistance from Z.H.Z. (Zhi-Hui Zhang), Y.D.Y., and J.P.Y. All authors discussed the results and commented on the manuscript.

Competing interests
The authors declare no competing interests.

Additional information
Supplementary information The online version contains supplementary material available at https://doi.org/10.1038/s41467-025-58590-z.

Correspondence and requests for materials should be addressed to Kong-Qiu Hu or Wei-Qun Shi.

Peer review information *Nature Communications* thanks Spyros Perlepes and the other anonymous reviewer(s) for their contribution to the peer review of this work. A peer review file is available.